MICROSTRUCTURE FORMATION IN THE POWDER HIPED HARDFACING ALLOY TRISTELLE 5183 (FE-21%CR-10%NI-7.5%NB-5%SI-2%C IN WT.%)

M.J. Carrington[a] D.G. McCartney[a] P.H. Shipway[a] D.A. Stewart[b]

[a] Advanced Materials Group, Faculty of Engineering, University of Nottingham,
Nottingham, NG7 2RD, UK
[b] Rolls-Royce plc, UK

HIGHLIGHTS

- HIPing homogenises the rapidly solidified powder microstructure of the alloy.
- Insufficient recrystallisation of the powder results in a bimodal matrix grain size.
- A mainly austenitic iron matrix contains NbC and M_7C_3 precipitates.
- M_7C_3 is largely suppressed in the powder but precipitates out during HIPing.

ABSTRACT

Tristelle 5183 (Fe-21%Cr-10%Ni-7%Nb-5%Si-2%C in wt%) is an alternative material to cobalt-based alloys for wear resistant hardfacing applications. In this work, gas atomised powder was consolidated by hot isostatic pressing (HIPing) at $1120 \pm 10\ ^{o}C$ which is $\sim 100\ ^{o}C$ below the melting onset point. The microstructure formation in the alloy, following densification, was investigated using X-ray diffraction, scanning and transmission electron microscopy and electron backscatter diffraction. The hot isostatically pressed (HIPed) alloy contains principally fcc γ-Fe, NbC, and M_7C_3 with a small fraction of bcc α-Fe and a π-ferrosilicide phase. This contrasts with the metastable gas atomised powder microstructure in which M_7C_3 formation is largely suppressed and NbC precipitation is reduced. Following HIPing, a wide distribution of γ-Fe grain sizes is found. The larger grains exhibit sub-grain structures with significant intra-grain misorientations as identified by kernel average misorientation (KAM) maps. The smaller grains ($< 10\ \mu$m) contain annealing twins, indicating that recrystallization had occurred only in certain localised regions which underwent sufficient plastic deformation in the early stages of HIPing. The work demonstrates the potential for HIPing hardfacing alloys to achieve a fine scale homogeneous microstructure.

KEYWORDS

- Fe-based Hardfacing
- Hot isostatic pressing
- Transmission electron microscopy
- Recrystallisation
- Powder metallurgy
- Carbide precipitation

1. INTRODUCTION

^{59}Co-based Stellite^{TM} hardfacings alloys are used extensively in the nuclear industry because of their excellent resistance to wear, corrosion and tribocorrosion [1]. However, when used in the primary circuit of pressurized water reactors (PWRs), ^{59}Co is transmuted to the γ-emitting isotope ^{60}Co (half-life: $\sim$ 5.3 years) which is a major source of radiation exposure for plant and maintenance workers [2,3]. Hence, Fe-based hardfacing alloys are being sought as alternatives [4]. Fe-based hardfacings are typically Fe-Cr-Ni-Si-C alloys that may also contain elements such as Mn, Mo, N and Nb and normally have a principally austenitic fcc or duplex fcc/bcc matrix which surrounds hard second-phase particles such as transition metal carbides or nitrides [5–7]. The principle of conferring wear resistance by the incorporation of hard phase in a ductile matrix is, in simple terms, similar to Stellite alloys, in which a Co-rich matrix is reinforced by the presence of chromium carbides.

Tristelle 5183 (Fe-21%Cr-10%Ni-7.5%Nb-5%Si-2%C in wt. %) is one of a small number of hardfacings developed specifically for nuclear applications. Its composition was first reported in a patent by Crook [8] who claimed it was suitable for nuclear hardfacing applications when deposited as a weld overlay. Subsequently, Burdett [9] tested a range of alloys at 300 ^{o}C and reported that the threshold galling load of Tristelle 5183 was such that it was a promising candidate to replace Stellite 6 in the primary circuit of a PWR. Burdett also reported that Tristelle 5183 performed well during sliding wear and corrosion testing in an environment representative of the primary circuit water chemistry. Likewise, during laboratory wear and corrosion screening tests with a simulated PWR primary circuit environment, Shiels et al. [10] concluded that the sliding wear behaviour of weld deposited Tristelle 5183 was generally comparable to that of Stellite 6 and that it exhibited an acceptable corrosion resistance. Further studies by, for example, Cockeram [11], and EPRI [12] reached similar conclusions. In a more recent study [13], EPRI compared the galling and sliding wear characteristics of HIPed 5183 and Stellite 6 in air at 343 ^{o}C and demonstrated the former was a potential alloy to replace

Stellite 6 in PWR applications. However, HIPed Stellite 6 and Tristelle 5183 exhibit fundamentally different tribological characteristics [13, 14], thus indicating that a deeper understanding of the microstructural features of the latter is crucial to improving its performance.

Traditionally, wear resistant hardfacings have been applied to component surfaces (typically 316 stainless steel) via weld or laser cladding. However, defects such as pores and cracks are difficult to eliminate and dilution with the substrate can adversely affect the properties of the hardfacing. Given the safety critical nature and long design lives required of reactor components, the production of hardfacings by powder HIPing, followed by diffusion bonding to a substrate alloy, is becoming the favoured manufacturing route for hardfaced components. The process of powder hot isostatic pressing (HIPing) involves the application of high temperature and pressure to powder held within a hermetically sealed container. Under appropriate conditions alloy powders can be consolidated and porosity eradicated. This approach offers advantages including better chemical and microstructural homogeneity and fewer defects compared to more traditional hardfacing processes [15]. It is reported that these advantages confer both improved corrosion and wear resistance to the hardfacing alloy [16].

There currently exists very little published work which details the microstructure formation of this complex multicomponent alloy when produced by powder HIPing [17, 18]. This paucity of information significantly hinders the more widespread deployment of powder HIPed Tristelle 5183 components as hardfacings. In a previous paper the authors reported the microstructure formation in gas atomised Tristelle 5183 powder [19]. The aim of the present work was to characterise the microstructure formation and the phase evolution which takes place during powder HIPing using X-ray diffraction, scanning electron microscopy (including electron backscattered diffraction), and transmission electron microscopy. HIPing of multicomponent gas-atomised powders can lead to the formation of non-equilibrium microstructures; therefore, the present work is important as it will provide a deeper understanding of how the microstructure evolves during such processing.

2. MATERIALS AND METHODS

2.1. MATERIALS

Tristelle 5183 powder was supplied by LSN Diffusion Ltd. (Ammanford, SA18 3GY, UK). The powder was manufactured using nitrogen gas atomisation to give a near-spherical powder particle morphology with a particle size typically < 500 μm. The powder was classified prior to HIPing into $60 - 150$ μm sized powder particles. The chemical composition is reported in Table 1 and was measured by LSN Diffusion Ltd. using inductively coupled plasma (ICP) spectrometry and Leco combustion analysis for the measurement of carbon and nitrogen.

The powder was HIPed into cylindrical bar (30 mm ⌀ x 200 mm) in mild steel canisters at Bodycote HIP Ltd (Carlisle Close, Sheffield Road, Sheepbridge, Chesterfield, S41 9ED). Powder HIPing was carried out at 1120 ± 10 ^{o}C and 103 ± 5 MPa with a dwell time of 240-270 min and a heating and cooling rate of 3.4-5.5 $^{o}C/min$ (certificate of conformity in accordance to EN 10204: 2004 3.1). After powder HIPing, the mild steel canisters were machined away. Cross-sectional discs for metallurgical examination were machined from the HIPed bars using electrical discharge machining (EDM) and subsequently ground on the flat faces to remove any recast layer associated with the EDM. The macrohardness of the alloy was 350 ± 1 HV 20 (n = 8).

Table 1: Chemical composition of ($60 - 150$ μm) Tristelle 5183 powder as determined by ICP and combustion analysis.

	Element %							
	Fe	**Cr**	**Ni**	**Nb**	**Si**	**C**	**N**	**Other**
wt%	Bal.	21.72	10.39	6.90	4.67	2.08	0.05	0.73
at%	Bal.	21.07	8.93	3.75	8.40	8.75	0.17	0.63

2.2. MICROSTRUCTURAL CHARACTERISATION

X-ray diffraction patterns were recorded from both the atomised powder and the HIPed alloy. XRD of the powder was performed on the as received powder ($60 - 150\ \mu$m). HIPed samples were ground, diamond polished to a 1 μm finish, and then given a final polish using 0.06 μm colloidal silica prior to analysis by X-ray diffraction (XRD) and microstructural analysis. The X-ray difractograms used for phase identification and Rietveld analysis were recorded using a Bragg-Brentano (θ-θ) configured Bruker D8 employing Cu K-α radiation and a LYNXEYE XE-T position sensitive (1D) energy discriminating detector. This machine is equipped with a variable anti-scatter screen, variable divergent slits, and a variable detector window. It was operated with a working voltage and current of 40 kV and 40 mA respectively. Scans were performed with a step size of 0.02^o between 20 and 120^o 2θ. Rietveld refinements [20] were performed using Topas V6 and the fundamental parameters approach to X-ray line profile fitting was employed [21,22].

A Nikon Eclipse LV100ND optical microscope was used to examine HIPed polished samples that were etched using a mixture of 10 ml nitric acid, 10 ml acetic acid, 15 ml hydrochloric acid, and 2-5 drops of glycerol. For microstructural analysis in the SEM, the powder samples were mounted in conductive resin, and prepared in accord with the metallurgical preparation steps outlined above. HIPed and powder samples were examined using backscattered electron (BSE) imaging and energy dispersive X-ray spectroscopy (EDX) in a FEI Quanta 600 scanning electron microscope operating at 20 kV. Electron backscatter diffraction (EBSD) data were acquired from HIPed samples using a Jeol 7100F field emission gun SEM (FEG-SEM) operating at 15 kV equipped with a Oxford Instruments Nordlys Nano EBSD detector. Electron transparent ($\sim$ 150 nm thick) transmission electron microscope (TEM) lamellae were prepared from HIPed samples using a FEI Scios DualBeam and a standard focused ion beam (FIB) lift-out method was employed. Conventional parallel beam TEM, scanning transmission electron microscopy (STEM) and EDX in the TEM was undertaken using a FEG source FEI Talos F200X TEM operating at 200 kV.

2.3. CALCULATION OF PHASE EQUILIBRIA

Thermodynamic modelling of phase equilibria was performed using Thermo-Calc® software [23] which is based on the CALculation of PHAase Diagram (CALPHAD) method [24]. The TCFE9 thermodynamic database (Thermo-Calc 2021) was employed and the elements included in the calculation were: Fe, Cr, Ni, Nb, Si and C. A limitation of the equilibrium calculations is that the composition of the alloy places it at the recommended composition limit for Si (5 wt. %) and just above the limit for Nb (5 wt. %) when using the TCFE9 database. This could affect the overall accuracy of the calculations.

3. RESULTS

3.1. PHASE IDENTIFICATION USING XRD

Fig. 1 shows X-ray diffractograms for both powder and HIPed material. The gas atomised powder is composed of a fcc austenitic γ-Fe solid solution (Fm3m space group) as the principal phase along with a smaller fraction of a bcc ferritic α-Fe solid solution (Im3m space group). The powder pattern also exhibits a complex set of reflections indicating the presence of a B1 (Fm3m) NaCl-type, fcc MX carbonitride (M = metal atom, X = C,N) with a lattice parameter close to that of NbC. As discussed in a previous paper, these reflections can be interpreted as coming from three crystalographically distinguishable populations of MX phase (indexed as different shades of green markers in Fig. 1) [19]. Likewise, an additional two sets of reflections, crystallographically consistent with an intermetallic π-phase (π-ferrosilicide), are observed in the powder diffraction pattern [19]. This phase is cubic and isostructural to $Fe_5Ni_3Si_2$ and $Cr_3Ni_5Si_2$ ($P2_13$) [25–27]. The powder diffractogram also contains several broad low intensity reflections which indicate the presence of a very small fraction of an orthorhombic M_7C_3 type carbide.

The X-ray diffractogram from the HIPed alloy reveals an fcc austenitic γ-Fe solid solution (Fm3m space group) as the major phase with smaller amounts of the following phases: orthorhombic M_7C_3 type carbide (basic structure in the Pmcn space group); MX type B1 phase (Fm3m space group with a lattice parameter extremely close to that of NbC); bcc ferrite α-Fe (Im3m space group); and traces of the cubic π-ferrosilicide phase referred to above and reported by Bowden et al. [25] ($P2_13$ space group). The phase fractions and the lattice parameters of the phases in the HIPed material were determined via Rietveld analysis and are listed in Table 2.

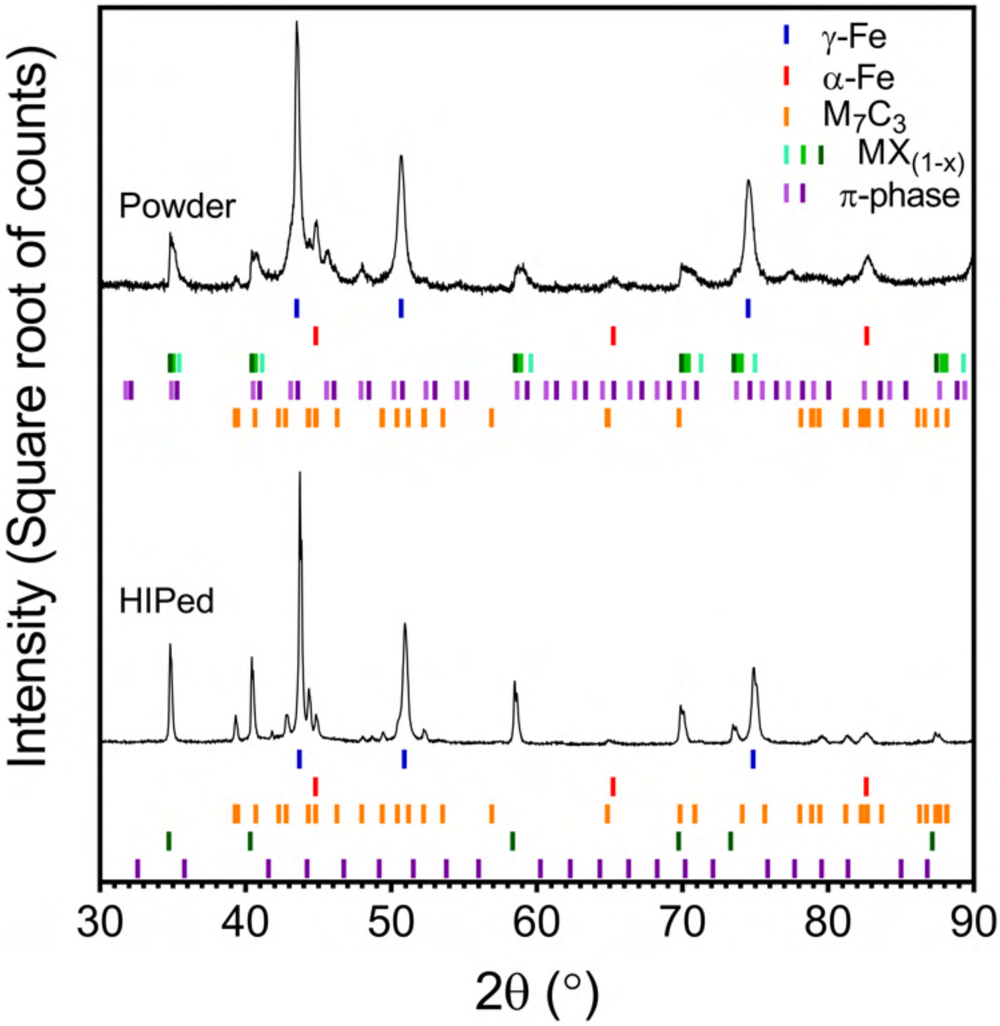

Figure 1: X-ray diffractograms obtained from gas atomised powder and the polished surface of the HIPed alloy. The powder exhibits reflections from γ-Fe (fcc), α-Fe (bcc), two distinctly different types of π-phase (indexed as different shades of purple), three crystallographically distinguishable forms of MX phase (shown as different shades of green), and evidence of M_7C_3. The HIPed alloy exhibits reflections from γ-Fe (fcc), M_7C_3, MX, α-Fe (bcc), and a trace of π- phase.

3.2. MICROSTRUCTURAL CHARACTERISATION

The microstructure of the gas atomised powder was reported in a previous paper [19] and is only brielfy summarised again here for completeness. Fig. 2 (a) and (b) show backscattered electron (BSE) images of powder particle cross-sections. The bright contrast features, which EDS showed to be a Nb-rich phase, are populations

Table 2: Phase fractions and lattice parameters (HIPed only) of the phases identified in Tristelle 5183 as determined by Rietveld analysis.

	γ-Fe	**M_7C_3**	**MX**	**α/δ-Fe**	**π-ferrosilicide**
Powder phase fractions (vol.%)	65-68	<6	5-6 (total)	6-8	15-17 (total)
HIPed phase fractions (vol.%)	74-76	13-14	10-11	1-2	<1
lattice parameters - HIPed alloy (nm)	a = 0.3586	a = 0.4506 b = 0.7001 c = 1.2128	a = 0.4462	a = 0.2859	a = 0.6131

of the MX phase identified by XRD and will be referred to as NbC throughout the rest of the paper. The single large $\sim 10\ \mu$m-sized NbC particle in Fig. 2(a) will be termed a pre-existing carbide. From its size and rounded morphology, this large carbide particle was present in the alloy melt prior to atomisation. The approximately micron-sized NbC particles in Fig. 2(a) and (b) will be referred to as primary carbides. These form a fine scale distribution of faceted crystals throughout the powder particle and are contained within a dendritic network (Fig. 2(b)). Nanoscale NbC particles are also evident in the interdendritic regions (Fig. 2(b)) and will be termed secondary carbides. Both the primary and secondary carbides formed during the rapid solidification of the powder. Fig. 2 shows that the matrix of the powder particles contain a number of dendritic grains which form during rapid solidification. In accord with XRD, these dendritic grains are presumed to be γ-Fe with contrast variation arising from channelling contrast as well as a small fraction of α-Fe. The interdendritic phase regions, indicated by the red arrows, correspond to the π-ferrosilicide phase identified by XRD [19].

An optical micrograph of the etched HIPed alloy is shown in Fig. 3. Large ($\sim$ 5 - 20 μm) precipitates are prevalent throughout the microstructure and these features are presumably the large NbC particles seen in the powder (Fig. 1). The etching also reveals discontinuous chains of heavily etched, micron-sized, dark contrast features which could be either pores and/or oxide particles. Such features are commonly found following the HIPing of gas atomised powders. They are termed prior particle boundaries (PPBs) and are attributed to gas porosity and/or undesirable precipitate formation at interfaces between powder particles formed during the HIPing cycle. [16]. Etching has also clearly revealed some matrix phase

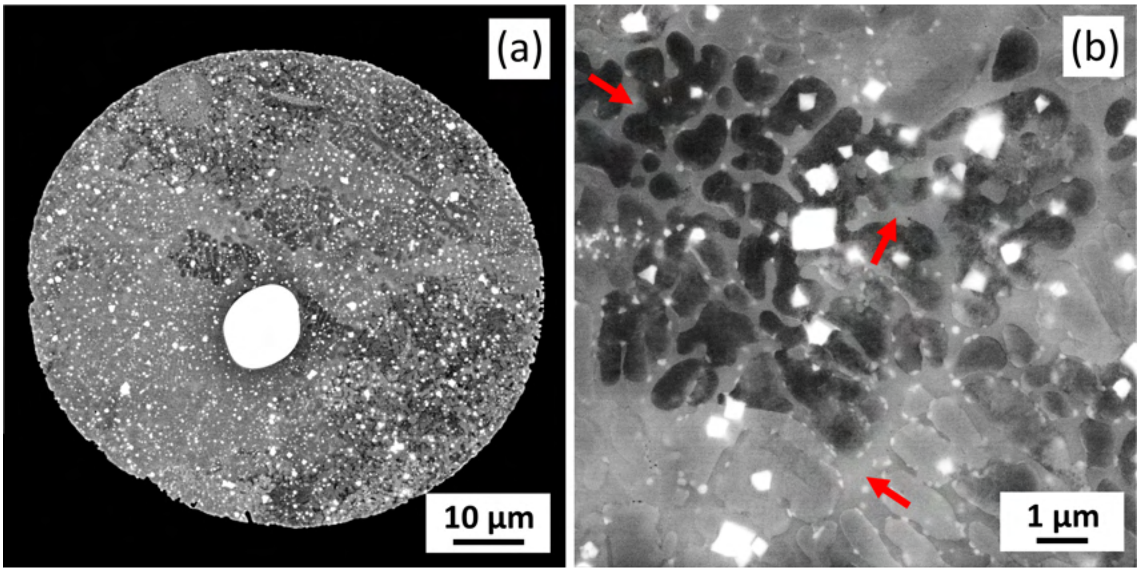

Figure 2: BSE micrographs showing the microstructural detail of gas atomised powder.(a) shows a dentritic matrix, a rounded pre-existing NbC particle and a uniform distribution of faceted primary NbC precipitates. (b) is a higher magnification BSE micrograph depicting micron-sized primary NbC precipitates and secondary nanoscale NbC particles in the interdendritic regions (red arrows).

grain boundaries within prior individual powder particles.

Representative BSE-SEM micrographs of the HIPed microstructure are shown in Fig. 4 (a-c) with EDX maps, Fig. 4 (d-h) which are from the same region as Fig. 4 (c). The matrix and the carbide precipitate phases are clearly distinguishable and can be correlated with the phases identified by XRD (Fig. 1). The bright-contrast features in the BSE micrographs (Fig. 4 (a-c)) are clearly Nb-rich (Fig. 4 (h)) and are thus consistent with the MX (NbC) phase (Fig. 1). This phase has a bimodal size distribution and the majority of the precipitates are < 2 μm in size and have a somewhat spheroidised morphology. However, a small number are significantly larger, ranging in size between $\sim$ 5 - 20 μm, and exhibit a combination of both globular and angular morphologies (Fig. 4 (a)). The larger MX (NbC) particles are believed to have formed in the melt alloying stage (prior to gas atomisation), whereas the finer ones precipitate out either during rapid droplet solidification or during the HIPing thermal cycle [19]. The dark contrast features ($\sim$ 1-5 μm in size) evident in Fig. 4 (a-c) are Cr-rich (Fig. 4 (e)) and correspond to the M_7C_3 phase. This phase is not observed in the gas atomised powder and must therefore

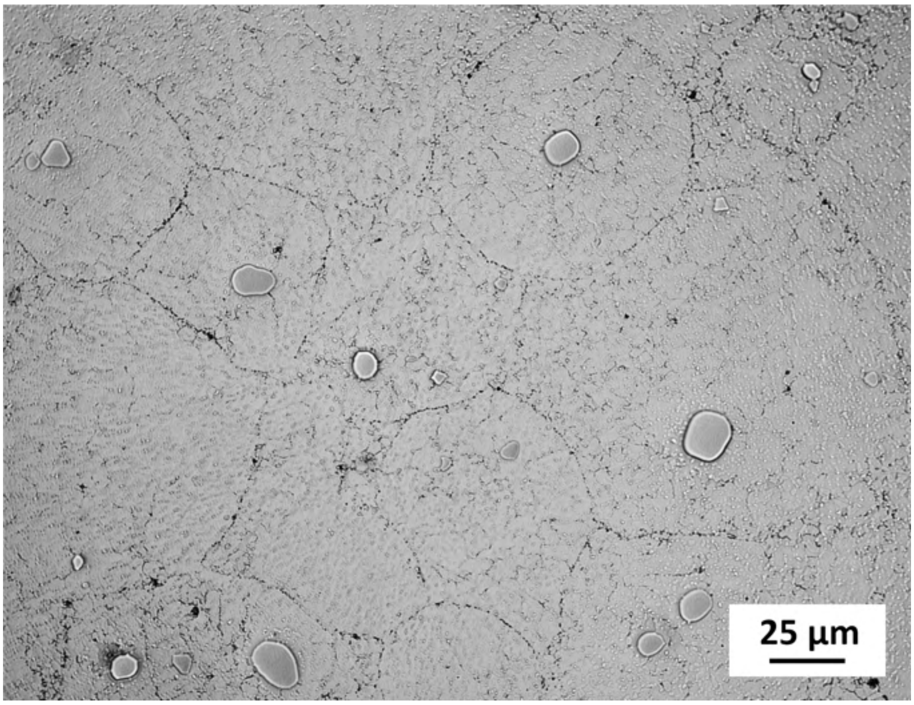

Figure 3: Optical micrograph of the HIPed alloy following etching - revealing prior particle boundaries, large NbC precipitates up to 20 microns in size, a network of finer scale precipitates and matrix phase grain boundaries.

have precipitated during HIPing [19]. Based on the phase fractions identified in XRD, the grey contrast matrix is principally an fcc (γ) Fe-based solid solution with contrast variation arising from channelling contrast as well as possibly a small fraction of a bcc (α) Fe-based solid solution and π-ferrosilicide. The small fraction of the π-ferrosilicide phase can be identified from the EDX maps as the Si- (Fig. 4 (f)) and Cr-rich (Fig. 4 (e)), and Fe-depleted (Fig. 4 (d)) regions relative to the surrounding matrix (white circles). Inspection of the BSE micrographs (Fig. 4 (a-c)) shows that the matrix grain size has a wide distribution, and whilst the average grain size is small, some grains are large relative to the other microstructural features within the HIPed alloy.

Fig. 5 (a), (b) and (c) show an EBSD-derived phase map, an inverse pole figure (IPF) map and a kernel average misorientation (KAM) map respectively of a representative region of the HIPed alloy. As previously identified by XRD and SEM, the alloy (Fig. 5 (a)) is principally composed of a Fe-based austenitic (fcc) solid solution (blue (γ-SS)) which surrounds both M_7C_3 (yellow) and Nb-based

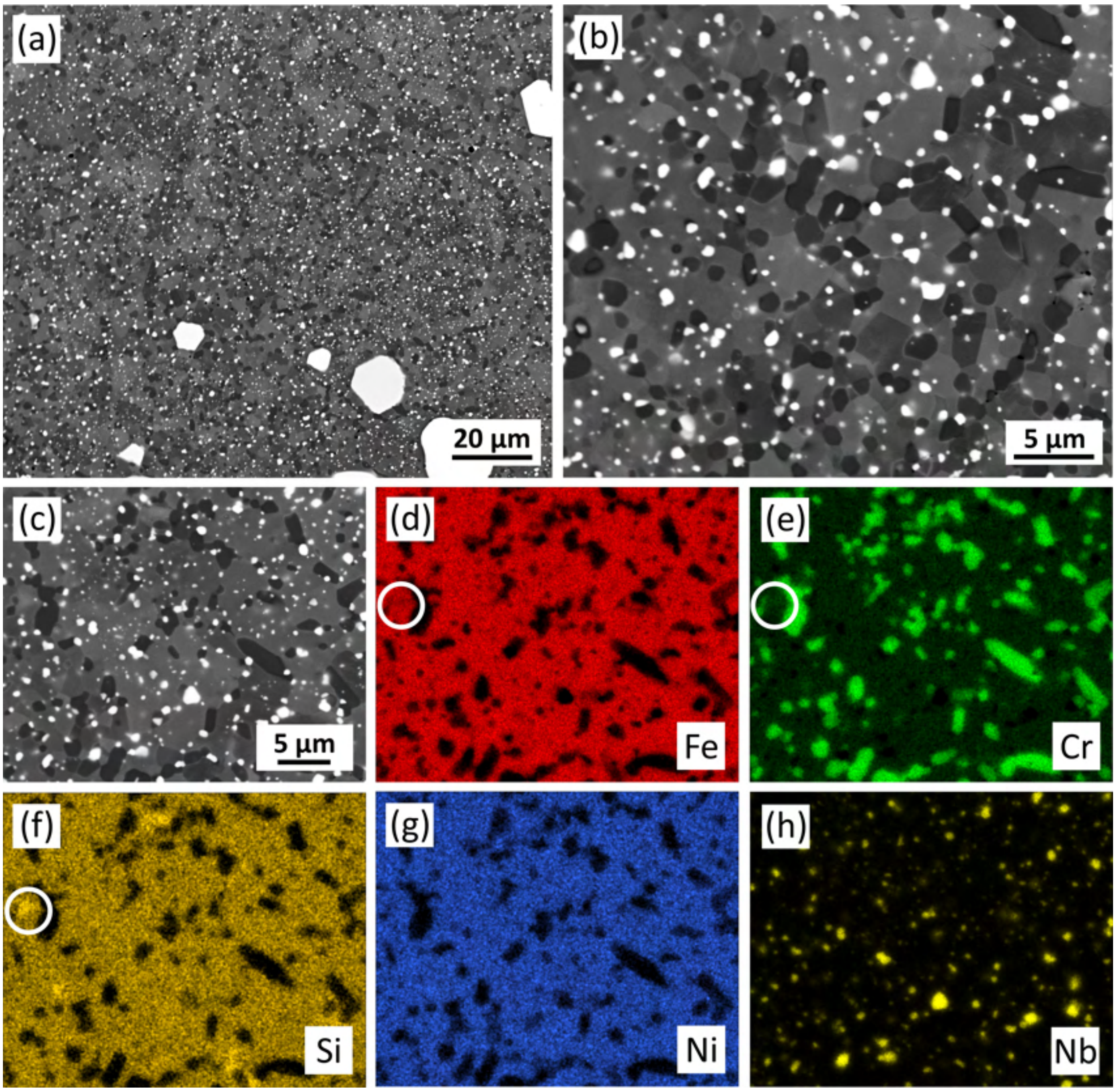

Figure 4: BSE-SEM micrographs (a-c) and EDX maps (d-h) depicting the microstructural detail of the HIPed alloy. The BSE-SEM micrographs show NbC precipitates (bright contrast), M_7C_3 carbides (darkest contrast) and matrix grains (varying grey contrast) which are principally γ-Fe. The EDX maps (d), (e), (f), (g) and (h) are from the same region as shown in (c) and are are maps for Fe, Cr, Si, Ni and Nb respectively.

MX (NbC) (green) precipitates. Smaller fractions of ferrite (red (α-SS)) and the π-ferrosilicide phase (pink) have also been identified by EBSD and both these phases have a precipitate size typically < 2 μm. It is also noted that these two precipitate phases often reside adjacent to one another. The compositions of numerous (n = 6) γ grains (identified by EBSD) were measured using EDX and the averaged composition is reported in Table 3.

The inverse pole figure orientation map (Fig. 5 (b)) shows that the γ solid solution matrix phase has a wide grain size distribution. Specifically, several regions with distinctly different grain sizes and morphologies are present within the microstructure (Fig. 5 (b)). These separate regions can be segregated into two broad categories, namely: (i) recrystallised matrix regions characterised by typically smaller (< 10 μm) equiaxed matrix grains with annealing twins (characteristic of recrystallisation), and (ii) non-recrystallised regions which generally contain larger grains. Fig. 5 (b) also shows that the larger grains typically exhibit large intra-grain misorientaions, seen as colour variation within an individual grain. The (KAM) map, showing the local orientation changes in the γ grains (Fig. 5 (c)), reveals the presence of extensive subgrain structures within the larger γ grains whereas, the smaller equiaxed grains appear, by comparison, to contain fewer internal misorientation substructures. It is also noted that the α-Fe and π-ferrosilicide precipitate phases are typically found within the recrystallised matrix regions.

Table 3: Composition of γ-Fe in the HIPed alloy as determined by EDX-SEM. The results are presented as the mean ± standard error of the mean (n=6).

	Fe	**Cr**	**Ni**	**Si**	**Other**
wt%	64.0 ± 0.2	16.1 ± 0.1	12.7 ± 0.1	6.3 ± 0.1	0.9 ± 0.2
at%	60.0 ± 0.2	16.2 ± 0.1	11.3 ± 0.1	11.6 ± 0.1	0.9 ± 0.2

Representative features of the HIPed alloy are shown in the HAADF-STEM micrograph, Fig. 6 (a), and Fig. 6 (b-f) show the corresponding EDX-STEM maps from the same region. The microstructure comprises the Fe-based γ solid solution phase previously identified by EBSD (Fig. 5), the spheroidised dark contrast (< 2 μm) Nb-rich (Fig. 6 (f)) carbides, and bright contrast (~ 1 - 2 μm) Cr-rich (Fig. 6 (c)) M_7C_3 type carbides. Fig. 6 (a) also reveals the bright contrast elongated precipitates which are believed to be the π-ferrosilicide phase as they are rich in Si (Fig. 6 (e)) and Cr (Fig. 6 (c)) and depleted in Fe (Fig. 6 (b)) and Ni (Fig. 6 (d)) relative to the matrix. The compositions of the γ-Fe and π-ferrosilicide phases have been determined by EDX-STEM and reported in Table 4. The composition of the π-ferrosilicide phases is close to that reported by Bowden et al. [25].

Fig. 7 (a) shows a BF-STEM micrograph of the microstructural detail of a typical

Table 4: Composition in wt% of the γ-Fe phase and π-ferrosilicide phases in the HIPed alloy as determined by EDX-STEM. The results are presented as the mean ± standard error of the mean (n_γ = 6, n_π = 1).

Phase	**Fe**	**Cr**	**Ni**	**Si**
γ-Fe (wt. %)	66.1 ± 0.3	15.8 ± 0.2	12.0 ± 0.2	6.1 ± 0.1
π-ferrosilicide (wt. %)	54.7 ± 0.5	22.9 ± 0.4	11.5 ± 0.4	10.9 ± 0.4

M_7C_3 precipitate and Fig. 7(b) depicts an accompanying Cr EDX map of this same region. This M_7C_3 precipitate exhibits parallel striations due to stacking faults, as indicated by the dashed white line, and this heavily flawed microstructure is characteristic of the M_7C_3 precipitates in the sample. Fig. 7 (c) is a higher magnification BF-TEM micrograph of the same precipitate shown in Fig. 7 (a) and the accompanying SADP (Fig. 7 (d)) confirms that this precipitate is Cr-based M_7C_3 (Zone axis: $[4\bar{1}\bar{1}]$). This SADP exhibits streaking due to stacking faults in the $\{110\}$ planes (with fault vectors $\pm\frac{1}{2}(a \pm b)$) and the high intensity maxima superimposed on these streaks corresponds to the diffraction spots for the basic orthorhombic structure. However, the streaking is also somewhat continuous which is indicative of complete disorder in the stacking of polyatomic layers and additional spots are observed which are typical of volumetric planar disorder [28]. In light of the above, it is suggested that this SADP arises from regions where there is complete disorder in the stacking of layers and regions where there are blocks arranged in the basic orthorhombic sequence which are separated by planar faults. The stacking faults causing the streaking in Fig. 7 (d) relate to the defects which are perpendicular to these streaks in Fig. 7 (a) and (c). The compositions of numerous M_7C_3 precipitates were evaluated by EDX-TEM and the average atomic fractions of Cr and Fe which combine to form the M component of this phases were found to be 0.818 ± 0.04 and 0.182 ± 0.04 (mean ± standard error of the mean (n = 4)) respectively ($\sim$(0.82Cr0.18Fe)$_7C_3$).

Fig. 8 (a-c) show BF-STEM micrographs of the different morphologies of the π-ferrosilicide precipitates (dark contrast) in the HIPed alloy which form principally at grain boundaries (as plate-like features) (Fig. 8 (a and b)) or at triple junctions (Fig. 8 (c)). The plate-like morphology of the π-ferrosilicide phase was confirmed by various tilting experiments. Fig. 8 (d) is a SADP from the triple junction π-ferrosilicide precipitate shown in Fig. 8 (c) (at a different tilt) and indexed to a [213] zone axis of the π-ferrosilicide phase identified by Bowden et al. [25].

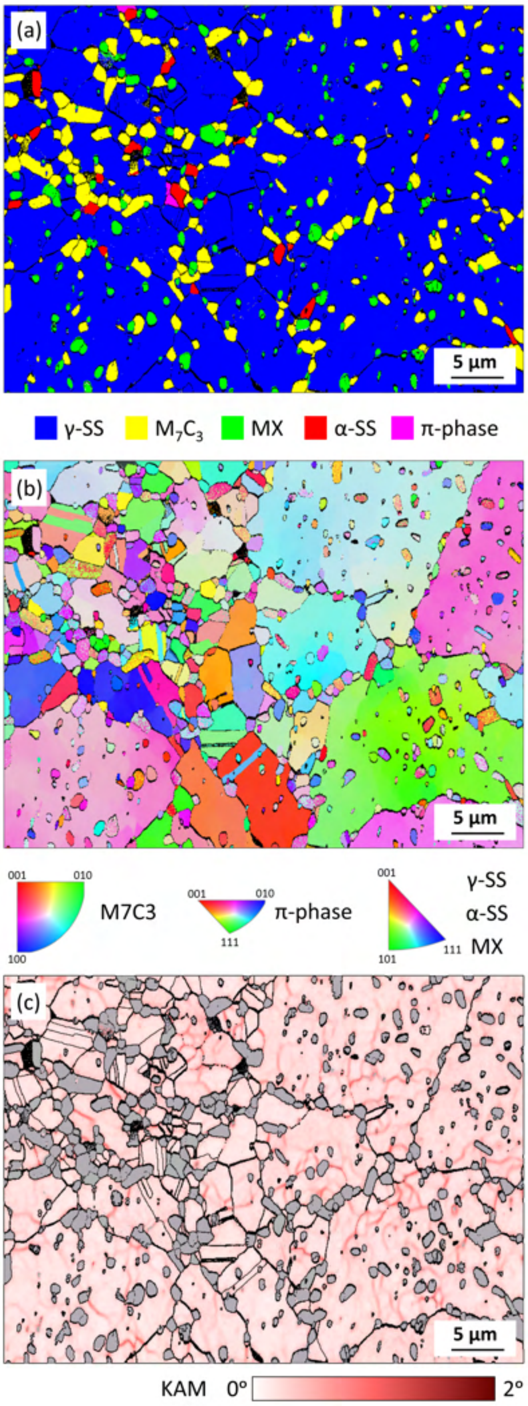

Figure 5: (a) is a representative EBSD-derived phase map of the HIPed alloy and depicts both M_7C_3 (yellow) and Nb-based MX (green) precipitates surrounded by an Fe-based austenitic matrix (blue) as well as a small fraction of ferrite and a π-ferrosilicide phase. (b) is a corresponding inverse pole figure (IPF) map showing the different grain sizes and morphologies which are present within the microstructure. (c) is a kernel average misorientation (KAM) map which reveals the intragrain localised misorientations subgrain structures of the γ-Fe grains, (other phases are shown in grey).

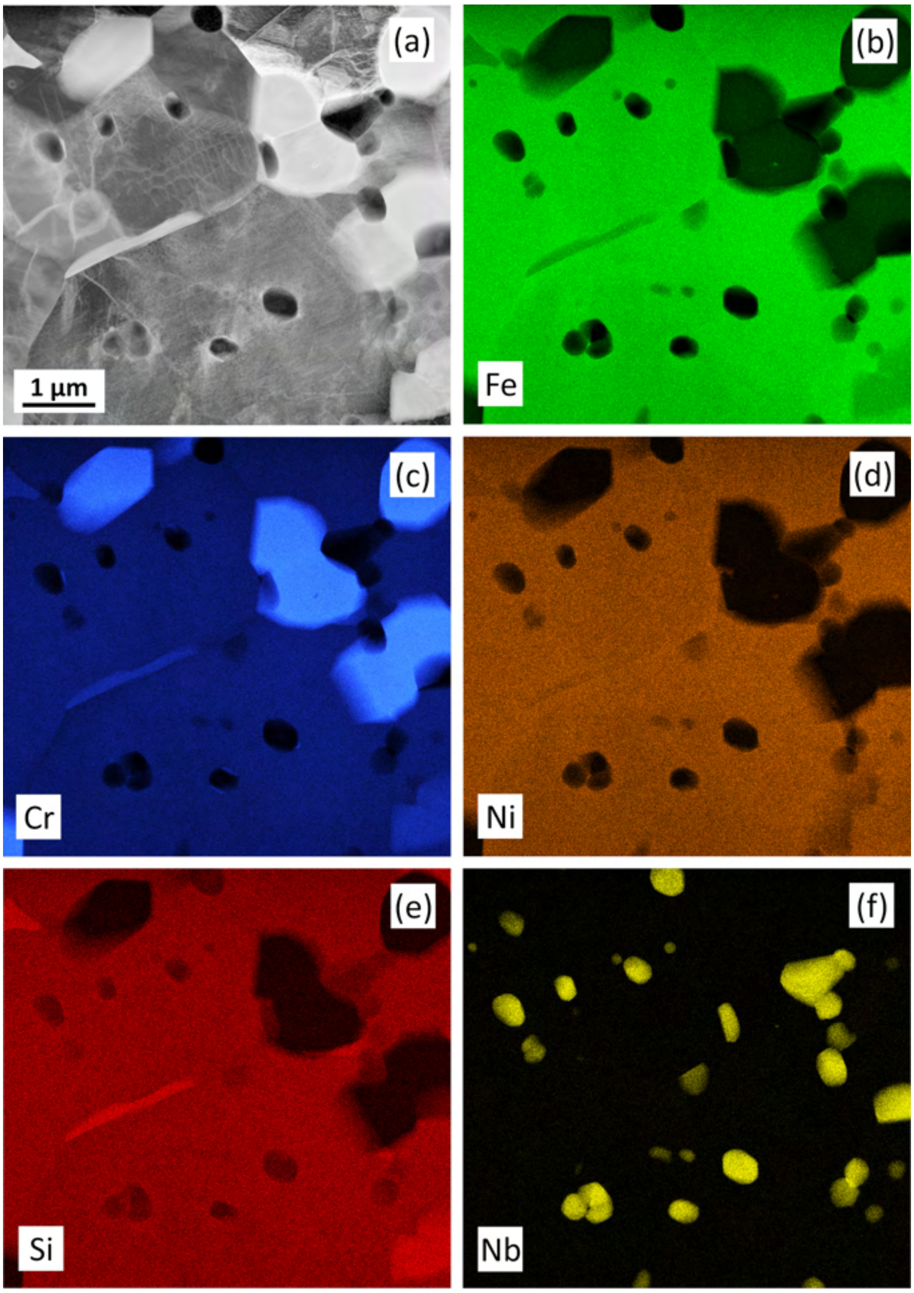

Figure 6: (a) HAADF-STEM micrograph of the HIPed alloy; (b), (c), (d), (e) and (f) are corresponding EDX maps for Fe, Cr, Ni Si and Nb respectively. (a) shows a grey contrast austenitic matrix with bright (Cr-rich (c)) and dark (Nb-rich (f)) contrast precipitates (M_7C_3 and NbC respectively) and (e) reveals the Si-rich π-ferrosilicide phase as an elongated precipitate.

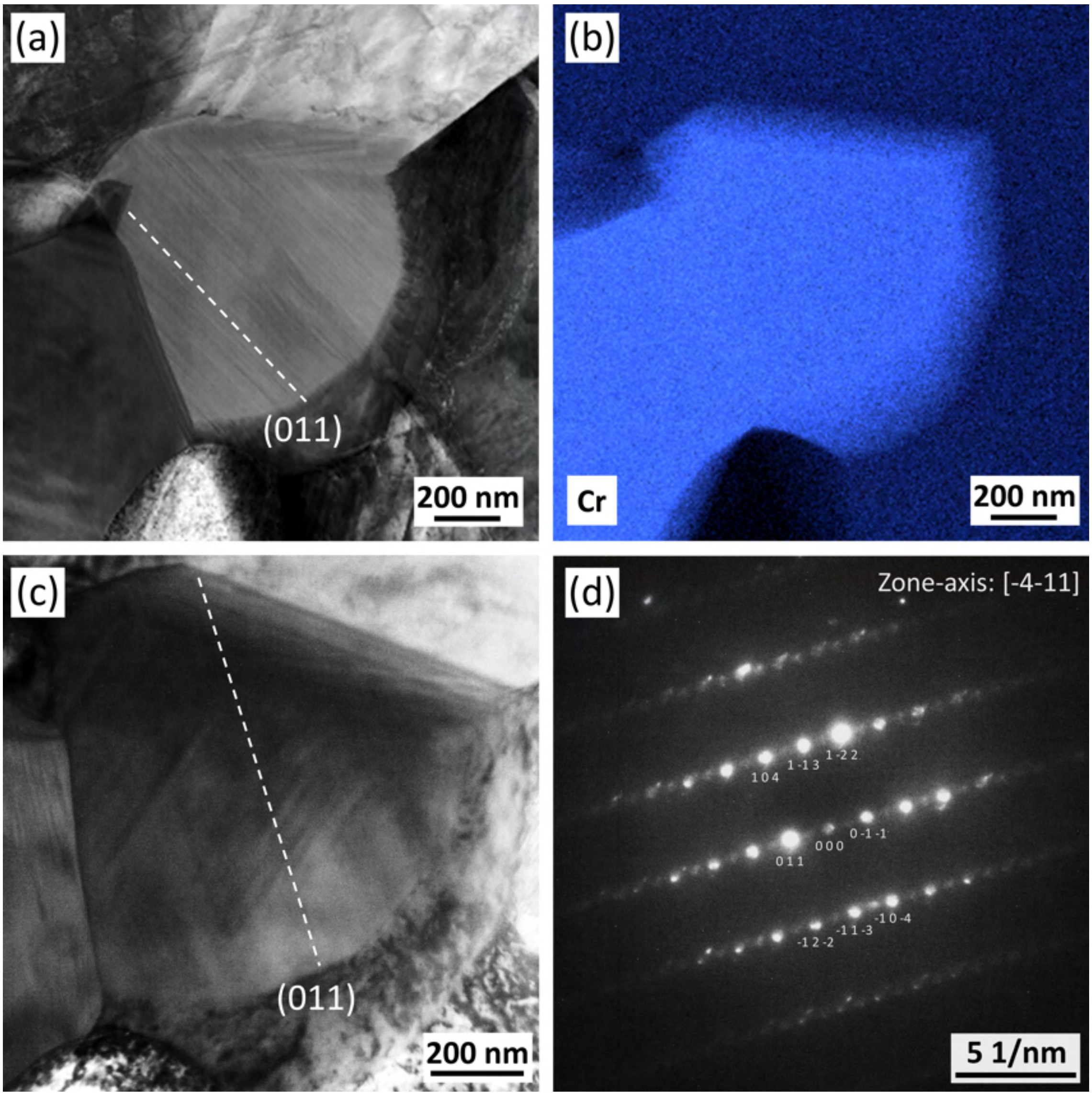

Figure 7: (a) representative BF-STEM micrograph showing the heavily flawed microstructure of the M_7C_3 precipitates in the HIPed alloy; and (b) corresponding EDX Cr map of this same region. (c) BF-TEM micrograph of the same precipitate as shown in (a) and (d) the SADP corresponding to (c).

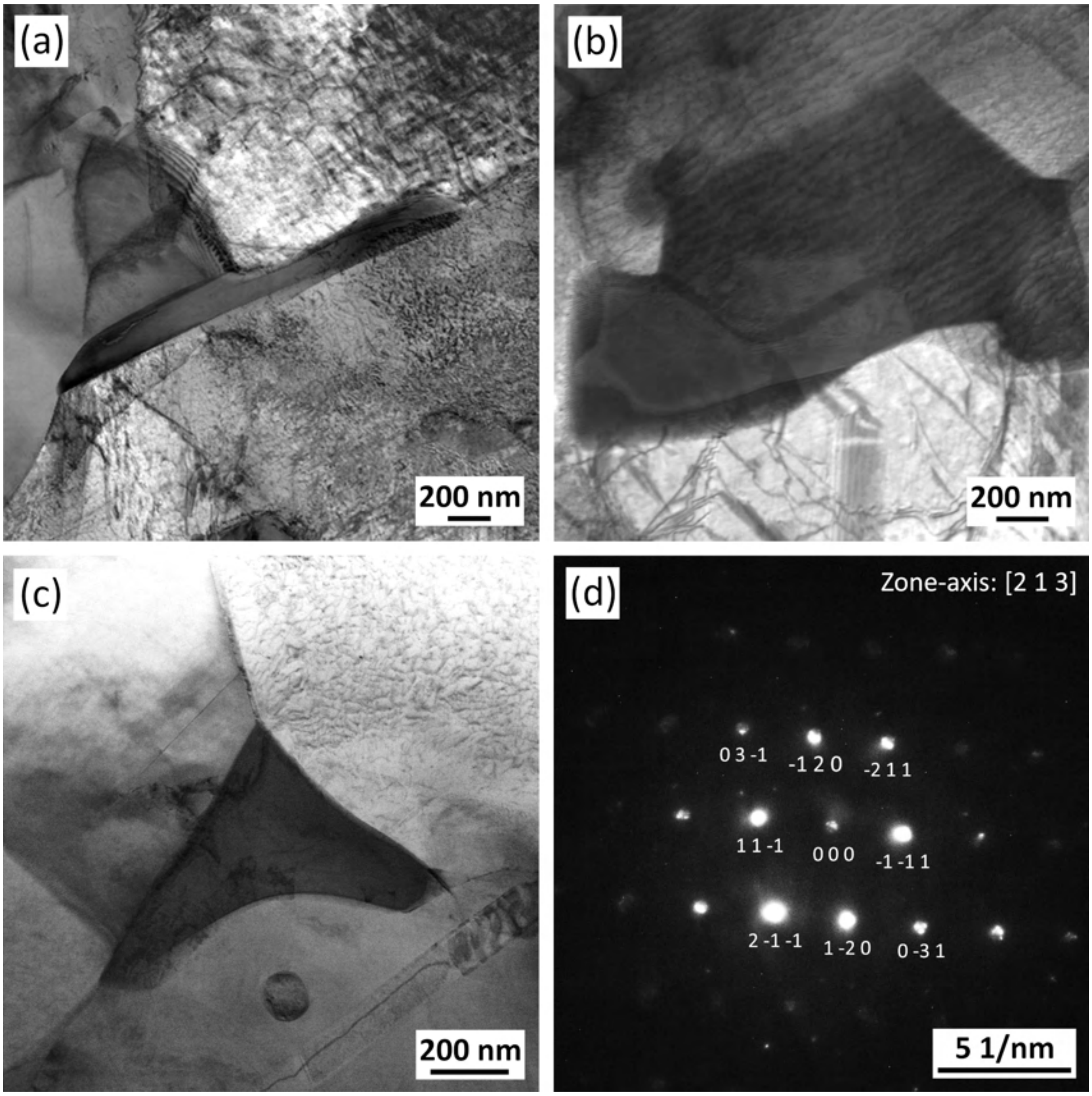

Figure 8: (a), (b) and (c) show BF-TEM micrographs depicting the morphologies of several different π-ferrosilicide precipitates of dark contrast within the microstructure. (a) and (b) show plate-like grains whereas (c) is a π-ferrosilicide grain at the triple junction. (d) shows a SADP from the triple junction π-ferrosilicide phase (at a different tilt to (c)) indexed to a [213] zone axis of the π-ferrosilicide phase.

4. DISCUSSION

Tristelle 5183 inert gas atomised powder was consolidated via HIPing at 1120 ^{o}C which is $\approx$ 100 K below the melting onset temperature of the alloy. This onset melting temperature was derived by differential thermal analysis (DTA), and these results are shown in Appendix A. It is evident that this largely homogenises the rapidly solidified metastable powder microstructure. Nevertheless, the microstructure and phase evolution during powder HIPing will now be considered in the following discussion.

4.1. PHASE EVOLUTION DURING HIPING

4.1.1. M_7C_3 precipitation

The HIPed microstructure of Tristelle contains approximately 13-14 vol% M_7C_3, whereas the formation of this phase is heavily suppressed in the gas atomised powder (Table 2). It is postulated that the M_7C_3 phase precipitates out predominantly during HIPing because its complex crystal structure means its nucleation and growth kinetics are slow. Fig. 7 (d) shows that the M_7C_3 phase has a "basic" orthorhombic structure (Pmcn space group) but it is extensively flawed with $\{110\}$ planar defects. This is in accord with the observations of Kowalski [28] and Morniroli et al. [29] and it is clear that the ideal stacking of polyatomic layers only extends over very small distances (Fig. 7 (a)). In accord with Kowalski [28], it is suggested that the greater part of the M_7C_3 crystal may be arranged differently, whereby disordered and ordered polytypic structures may be present in M_7C_3 which precipitates out during HIPing. As shown in Fig. 7 (d), the disorder in the stacking sequence is due to stacking faults in the $\{110\}$ planes. However, in ordered polytypic structures, regions which differ from the basic arrangement of polyatomic layers due to $\{110\}$ faulting are periodically repeated over large regions of the M_7C_3 crystal. Twinning is also reportedly prevalent in M_7C_3 crystals which involve three kinds of orthorhombic regions rotated through an angle of 120^{o} around the c axis [29]; however, this has not been directly observed in the present study.

4.1.2. NbC phase evolution

The total phase fraction of the NbC phase increases as a result of HIPing (Table 2) and it is clear, based on the phase and microstructural characterisation of HIPed and gas atomised Tristelle 5183 [19], that the NbC precipitates significantly evolve during HIPing. XRD (Fig. 1) shows that the HIPed alloy contains a single crystallographic population of the NbC phase (NbC) which exhibits sharp reflections; this is unlike the three distinctly different populations of NbC phase which are observed within the gas atomised powder (Fig. 1) [19]. The lattice parameter of the NbC phase in HIPed Tristelle 5183 is 0.4462 nm (as determined by Rietveld analysis (Table 2)) which is close to the value of 0.4469 nm given in the International Centre for Diffraction Data file (# 01-070-8416) for stoichiometric NbC. Therefore, during HIPing the NbC appears to be equilibrated and chemically homogenised even though this phase exhibits size and morphological variability within the HIPed microstructure (Figs. 3 to 5).

In the HIPed alloy, the NbC precipitates exhibit a bimodal size distribution with two distinctly different morphologies, namely: (i) < 2 μm sized somewhat spheroidised precipitates (Figs. 4 to 6), and (ii), large 5 - 20 μm sized crystals. The latter evolve from the melt processing stage prior to gas atomisation (Figs. 3 and 4) as discussed previously [19]. In contrast, three morphologically different NbC precipitates are observed in the gas atomised powder, more specifically: (i) nanoscale particles contained within the interdendritic and intracellular regions of powder particles, (ii) < 2 μm sized faceted crystals distributed throughout powder particles, and (iii) large 5 - 20 μm sized crystals.

It is proposed that the faceted and nanoscale precipitates present within the gas atomised powders evolve into the < 2 μm somewhat spheroidised precipitates during HIPing. This evolution is principally governed by two factors. Firstly, further NbC precipitation occurs from: (i) the matrix which is probably supersaturated with Nb and C, and (ii), the decomposition of Nb and C containing intermetalic phases found within the powder [19]. Secondly, due to the time spent at elevated temperature, the faceted and nanoscale NbC precipitates spheroidise and coarsen. Coarsening is driven by a reduction in the overall interfacial energy between matrix and NbC particles. The dependence of coarsening rate on the temperature dependent diffusion coefficient is well known [30, 31].

4.1.3. Silicide and ferrite evolution

Silicide precipitates reside at grain boundaries and triple junctions (often adjacent to one another) and are typically < 2 μm in size (Figs. 5 and 6). It is speculated that these are most probably solid-state precipitates which form during the cool down period of HIPing and that they largely did not form during the rapid solidification of droplets. Therefore, they are more likely to nucleate and grow at grain boundaries between the γ-Fe grains as this reduces the energy barrier to nucleation. There is also the possibility of grain boundary diffusion providing faster mass transport of the substitutional elements that are present in this phase. Given the clear relationship between the α-Fe and π-ferrosilicide precipitates, it is postulated that the π-ferrosilicide precipitates due to the decomposition of α-Fe.

The gas atomised powder contains a large fraction ferrite as well as the π-ferrosilicide phase which is rich in Cr, Nb, Si and C solute elements [19]. In accord with the observations made on the HIPed alloy in the present study, these phases must decompose and transform into M_7C_3, γ-Fe and NbC during the early stages of the HIPing cycle.

4.2. MATRIX RECRYSTALLISATION DURING HIPING

Fig. 5 has shown that the γ matrix microstructure can be subdivided into two broad categories, namely: (i) recrystallised regions composed of small (< 10 μm) equiaxed grains that are relatively free from internal misorientations and substructures which often contain annealing twins; and (ii), non-recrystallised regions composed of larger grains which contain high intra-grain misorientations and substructures. It is postulated that these regions can probably be related to the size of individual powder particles prior to HIPing and can be explained by the thermal treatment and the mechanical deformation that occurs during HIPing.

The following section will discuss the principal factors, relating to powder particle size, which influence recrystallisation during HIPing.

First, it needs to be noted that dynamic recrystallization occurs during the elevated temperature deformation of low to medium stacking fault energy alloys such as the matrix in Tristelle 5183 [32, 33] (Tables 3 and 4). Secondly, the driving force for dynamic recrystallisation is the amount of stored energy within the γ-Fe, more specifically, energy arising from lattice strains and the crystalline imperfections generated during deformation. During HIPing, plastic deformation dominates densification during the initial stages as the contact stresses between neighbouring particles are high enough for them to plastically yield.

The inhomogeneous plastic deformation incurred by a given powder particle in the initial stages of HIPing is dependent on particle size; smaller powder particles are generally plastically deformed more than larger ones [34–38] (Fig. 3). This is important as the stored energy generated due to plastic deformation in the initial stages of HIPing will influence the ability of a powder particle to undergo dynamic recrystallisation. Hence smaller powder particles are more likely to undergo complete (and/or partial) dynamic recrystallisation during HIPing.

It is suggested that the large γ grains observed in the HIPed microstructure most probably originate from larger powder particles and retain a phase and microstructural lineage with the dendritic structures observed in the gas atomised powders [19]. More specifically, the large non-equiaxed γ grains are morphologically comparable/similar to the γ dendritic grains observed in the gas atomised powder (Fig. 2) [19].

It is hypothesised that the sub-structures exhibited within the γ grains (Fig. 5) are principally a result of two factors, namely: (i) remaining features from the fine scale cellular and dendritic microstructures exhibited within the rapidly solidified gas atomised powders [19], and (ii), deformation structures generated during HIPing. These features are retained within the HIPed microstructure as a consequence of an insufficient homogenisation of the microstructure during HIPing and the inability of certain powder particles (and/or regions) to undergo dynamic recrystallisation. The presence of microstructural regions comprised of larger γ grains relating to typically larger powder particles which have not been subject to dynamic recrystallisation (Fig. 5) suggests that the as-received powder particles do not generally have enough stored energy to recrystallise without significant deformation. Therefore, the stored energy generated due to plastic deformation in the initial stages of HIPing is believed to be a prerequisite for dynamic recrystallisation in the later stages of HIPing.

Crucially, the above hypotheses imply that the microstructures generated during gas atomisation can directly influence the final HIPed microstructure of Tristelle 5183. A significant fraction of the microstructure is not completely recrystallised during HIPing (Figs. 4 and 5), and as larger powder particles are less likely to undergo the required plastic deformation for dynamic recrystallisation, the original microstructures of larger gas atomised powder particles are more likely to be partially retained within the HIPed microstructure. This concurs with the findings of Irukuvarghula et al. [34] who studied the HIPed microstructure of 316L and also explains the broad γ-Fe grain size distribution within HIPed Tristelle 5183 reported by Zhao et al. [18].

To summarise, plastic deformation in the early stages of HIPing is a prerequisite for recrystallisation because the as-received powder does not generally have enough stored energy to recrystallise without deformation. The plastic deformation incurred by a given powder particle is dependent on its size; therefore, the particle size distribution has a profound influence of the HIPed microstructure [34]. The plastic deformation incurred by a large fraction of powder particles in the early stages of HIPing is insufficient to permit dynamic recrystallisation during HIPing. However, the use of a higher HIPing temperature/pressure or extended holding time could generate a higher dislocation density and trigger more extensive recrystallisation. The metastable nature of powder particles prior to atomisation can significantly influence recrystallisation during HIPing. Hence, it is clear that powder characteristics play a critical role in the development of the HIPed microstructure.

4.3. CALCULATED PHASE EQUILIBRIA AND MICROSTRUCTURAL EVOLUTION

The metastable gas atomised powder was HIPed at 1120 ± 10 ^{o}C and 103 ± 5 MPa with a dwell time of 240-270 min and a heating and cooling rate of 3.4-5.5 ^{o}C/min. This allowed precipitation of NbC and M_7C_3, an increase in the fraction of the γ-Fe phase, along with the disappearance of δ-Fe and π-ferrosilicide phases which were in the original powder. Although the temperature/time/pressure conditions may have been insufficient for equilibrium to have been reached, it is still of interest to use the CALPHAD method to predict the equilibrium behaviour. This, along with careful interpretation, can provide significant insight into phase evolution as long as the thermodynamic models of the phases are sufficiently accurate for the temperature and composition ranges of interest.

The simplest representation of the phase equilibria is obtained by plotting a phase fraction versus temperature diagram as shown in Fig. 9 (a). This reveals a solidification sequence that is described in Eq. (4.1). The formation of primary NbC, followed by M_7C_3 precipitation from the melt at a lower temperature agrees with previous microstructural observations on Tristelle 5183 which was cast with a relatively slow cooling rate [19]. However, δ-Fe is predicted to be the initial matrix solid phase, whereas previous experimental observations reported this to be the γ-Fe phase during slow cooling [19].

The phase fractions of 50.2 % δ-Fe, 30.2 % γ-Fe, 8.7 % NbC and 10.9 % M_7C_3 in wt. % (50.7 % δ-Fe, 29.6 % γ-Fe, 8.2 % NbC and 11.5 % M_7C_3 in vol. %) predicted at the HIPing temperature of 1120 ^{o}C can be compared with the measured values obtained from the HIPed alloy (Table 2). There is very reasonable agreement for the quantities of carbide phases. The TCFE9 database does not contain a thermodynamic description of the π-ferrosilicide phase which is observed in only small quantities in the alloy.

The disparity in the calculated and measured amounts of δ and γ-Fe could be due to a number of factors, namely: (i) the transformation kinetics have not allowed equilibrium to be achieved; (ii) phase changes may have taken place during cooling from the HIPing temperature; and (iii), the thermodynamic models for phases may be insufficiently accurate for the compositional space investigated. In this respect, it is notable that calculations have been performed at and/or above the TCFE9 databases recommended composition limits for both Si (5 wt. %) and Nb (5 wt. %).

Nevertheless, it is valuable to explore the phase equilibria in a compositional space around that of the alloy. This will help evaluate general trends in phase stability and phase fractions, and could provide insight into the behaviour of the alloy. Therefore, isopleth diagrams were calculated for each of the main solutes as shown in Fig. 9 (b) and Appendix B. The vertical dashed line on each isopleth diagram indicates the composition of the alloy in this study. Fig. 9 (b) suggests that the phases present in the alloy are very sensitive to changes in Si content but less so with regard to the other solutes. To illustrate this further, Fig. 9 (c) shows the calculated variation in equilibrium phase fractions of δ and γ-Fe as a function of Si content along the isopleth line at the HIPing temperature of 1120 ^{o}C. These diagrams demonstrate that changes Si content by as little as ± 1 % can significantly alter the γ-Fe or δ-Fe phase fraction at the HIPing temperature. These diagrams also illustrate the steep slope of both the γ-Fe and δ-Fe phase boundaries with respect to temperature. The implications of this compositional sensitivity are that small errors in the parameters describing the thermodynamic properties of the fcc and bcc forms of iron could drastically alter predicted phase equilibria and account for the discrepancy between measured and calculated γ/δ-Fe proportions.

$$\begin{aligned} Liquid \rightarrow Liquid + NbC \rightarrow Liquid + NbC + M_7C_3 \\ \rightarrow Liquid + NbC + M_7C_3 + \delta\text{-}Fe \\ \rightarrow Liquid + NbC + M_7C_3 + \delta\text{-}Fe + \gamma\text{-}Fe \\ \rightarrow NbC + M_7C_3 + \delta\text{-}Fe + \gamma\text{-}Fe \end{aligned} \tag{4.1}$$

Clearly, a shift in the phase boundaries on the Si isopleth by as little as 1 - 1.5 % would place the alloy in a domain where the computationally predicted phase fractions at 1120 ^{o}C are in better agreement with the experimental values in Table 2.

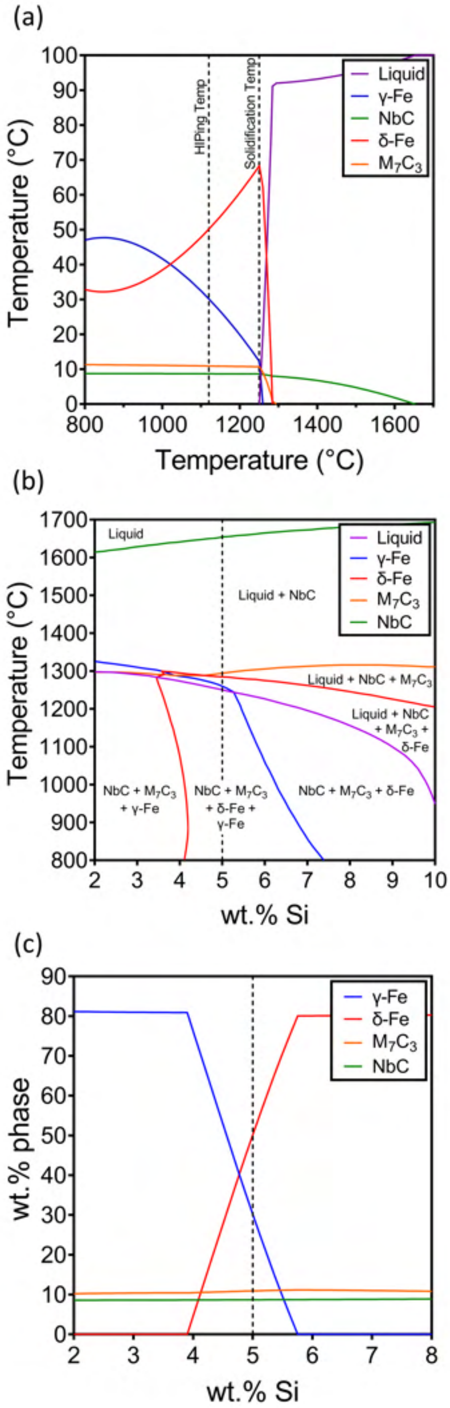

Figure 9: (a) Equilibrium phase fraction diagram for Tristelle 5183 calculated using the TCFE9 thermodynamic database. (b) Isopleth diagram showing the effect of Si and temperature on phase equilibria. All compositional variables are kept constant except two, namely, the element of interest (Si) and the base solvent (Fe). (c) Isothermal diagram calculated at the HIPing temperature (1120 ^{o}C) showing the effect of Si on the predicted equilibrium phase fractions.

Furthermore, the predicted solidification sequence would also agree more closely with the experiments reported in a previous paper [19]. It is therefore suggested that whilst the CALPHAD approach requires further improvement, it can still provide significant insight into phase evolution and phase stability if carefully interpreted and rationalised against experimental observations.

The HIPed microstructure is probably important from a tribological perspective as the carbide size, fraction and spatial distribution are factors which govern a materials adhesive wear behaviour [16,39–41]. In comparison with the alloy in its other forms, such as cast ([19]) or Plasma Transferred Arc (PTA) welded ([12]), the powder HIPed alloy has both a very fine matrix grain size and equiaxed carbide grain structure. The fine scale carbide precipitates are also homogeneously distributed within the austenitic matrix, and this reduces the effective matrix mean free path. This reportedly minimises the matrix-to-matrix contacts during sliding and so potentially improves adhesive wear resistance compared to cast or PTA weld overlays [39,41].

5. CONCLUSIONS

1. HIPed Tristelle 5183 is principally composed of an austenitic Fe-based solid solution matrix which surrounds Cr-based M_7C_3 (13-14 vol%) and Nb-based MX (10-11 vol%) secondary hard phase precipitates. Smaller fractions of ferrite (1-2 vol%) and a π-ferrosilicide phase (< 1 vol%) are also observed within the alloy.

2. The γ-Fe grain size in HIPed Tristelle 5183 is highly varied as the microstructure has not been completely recrystallised during HIPing and some regions within the microstructure retain a strong morphological and crystallographic relationship with the inert gas atomised powder. Inert gas atomised Tristelle 5183 powder does not generally have enough stored energy to dynamically recrystallise without significant plastic deformation in the initial stages of HIPing. The degree of plastic deformation and therefore ability of a powder particle to recrystallise is dependent on powder size.

3. Two distinctly different morphologies of NbC precipitate exist within the HIPed alloy, more specifically: coarse 5-20 μm sized precipitates which evolve from the melt prior to inert gas atomisation, and < 2 μm spheroidised precipitates which evolve during gas atomisation and HIPing. The evolution of the NbC precipitates during HIPing is governed by chemical homogenisation, equilibration, further growth via precipitation, coalescence and spheroidisation.

4. M_7C_3 carbide formation is largely suppressed in the gas atomised powder and precipitate out during HIPing with a basic orthorhombic crystal structure (Pmcn space group) that is largely flawed with $\{110\}$ planar crystallographic defects. The basic ideal stacking of polyatomic layers only extends over very small distances and the greater part of M_7C_3 precipitates may be arranged differently and exhibits both disordered and polytypic structures.

5. A π-ferrosilicide phase exists within the HIPed alloy in trace amounts and is

principally found at grain boundaries (as plates) or at triple junctions. This phase is spatially related to α-Fe and may precipitate due to the decomposition of α-Fe during the cool down period of HIPing.

ACKNOWLEDGEMENTS

The authors gratefully acknowledge funding from Rolls-Royce plc. M.J. Carrington also acknowledges funding from the Faculty of Engineering, University of Nottingham in support of a PhD studentship. The authors thank the Nanoscale and Microscale Research Centre (nmRC) for providing access to instrumentation. Access to the JEOL 7100F FEG-SEM was supported by the Engineering and Physical Sciences Research Council (EPSRC) [under grant EP/L022494/1] and the University of Nottingham. The authors also wish to thank Dr. Geoff West of the Warwick Manufacturing Group (WMG) at the University of Warwick for his technical assistance concerning TEM and TEM sample preparation. Dr. Jaimie Daure and Dr. Vilma Ratia-Hanby are also gratefully acknowledged for their technical assistance.

DATA AVAILABILITY

The raw/processed data required to reproduce these findings cannot be shared at this time as the data also forms part of an ongoing study.

BIBLIOGRAPHY

[1] Matthew John Carrington, JL Daure, Vilma Liisa Ratia-Hanby, Deen Zhang, Philip H Shipway, David A Stewart, and David Graham McCartney. Microstructural characterisation of subsurface deformation and the degradation of stellite 6 induced by self-mated sliding contact in a simulated pwr environment. *Tribology International*, 158:106899, 2021.

[2] H. Ocken. Reducing the cobalt inventory in light water reactors. *Nuclear technology*, 68(1):18–28, 1985.

[3] H. Ocken. The galling wear resistance of new iron-base hardfacing alloys: a comparison with established cobalt-and nickel-base alloys. *Surface and Coatings Technology*, 76:456–461, 1995.

[4] J.L. Sulley, I. Hookham, B. Burdett, and K. Bridger. Introduction of hot isostatically pressed, reactor coolant system components in PWR plant. In *International Conference on Nuclear Engineering*, volume 49330, pages 357–367, 2010.

[5] B.G. Mellor. *Surface coatings for protection against wear*. Woodhead Publishing, 2006.

[6] P. Aubry. Survey on Stellite substitutes for hardfacing in nuclear environments. Technical report, European Commission and Seventh Framework Programme, 2012.

[7] S. Atamert and J. Stekly. Microstructure, wear resistance, and stability of cobalt based and alternative iron based hardfacing alloys. *Surface engineering*, 9(3):231–240, 1993.

[8] P. Crook and R.D. Zordan. Nuclear grade steels, 1987. US Patent 4,643,767.

[9] W.B. Burdett. Development of cobalt free wear resistant alloys for nuclear applications. *Surface Engineering*, 8(2):131–135, 1992.

[10] S.A. Shiels, W.L. Wilson, K.W. Rosengarth, and G.L. Wire. Laboratory evaluation of low cobalt wear materials for nuclear applications. Technical report, Bettis Atomic Power Laboratory, 1994.

[11] B.V. Cockeram. Corrosion resistance and electrochemical potentiokinetic reactivation testing of some iron-based hardfacing alloys. *Corrosion*, 56(8):849–859, 2000.

[12] E.V. Murphy and I. Inglis. Endurance tests of valves with cobalt-free hardfacing alloys: PWR phase. Technical report, Electric Power Research Inst., 1992.

[13] J.A. Siefert and D.W. Gandy. Program on technology innovation: Galling and sliding wear test results for candidate hardfacing alloys manufactured by power metallurgy and hot isostatic pressing (pm/hip). Technical report, Electric Power Research Inst., 2013.

[14] J.L. Daure, M.J. Carrington, D.G. McCartney, D.A. Stewart, and P.H. Shipway. Measurement of friction in galling testing–an example of its use in characterising the galling behaviour of hardfacings at ambient and elevated temperature. *Wear*, page 203736, 2021.

[15] H.V. Atkinson and B.A. Rickinson. *Hot isostatic processing*. Springer, 1991.

[16] J. Sulley and D. Stewart. HIPed hard facings for nuclear applications: Materials, key potential defects and mitigating quality control measures. In *24th International Conference on Nuclear Engineering*. American Society of Mechanical Engineers, 2016.

[17] D.J. Bowden. *Assessment of cobalt-free hardfacing stainless steel alloys for nuclear applications*. PhD thesis, Department of Materials, The University of Manchester, 2017.

[18] C. Zhao, D. Stewart, J. Jiang, and F.P.E. Dunne. A comparative assessment of iron and cobalt-based hard-facing alloy deformation using HR-EBSD and HR-DIC. *Acta Materialia*, 159:173–186, 2018.

[19] M.J. Carrington, J. Daure, V.L. Ratia, P.H. Shipway, D.G. McCartney, and D.A. Stewart. Microstructural characterisation of Tristelle 5183 (Fe-21%Cr-10%Ni-7.5%Nb-5%Si-2%C in wt%) alloy powder produced by gas atomisation. *Materials & Design*, 164:107548, 2019.

[20] R.A. Young. *The rietveld method*, volume 6. Oxford university press Oxford, 1993.

[21] R.W. Cheary and A. Coelho. A fundamental parameters approach to X-ray line-profile fitting. *Journal of Applied Crystallography*, 25(2):109–121, 1992.

[22] R.W. Cheary, A.A. Coelho, and J.P. Cline. Fundamental parameters line profile fitting in laboratory diffractometers. *Journal of Research of the National Institute of Standards and Technology*, 109(1):1, 2004.

[23] J. Andersson, T. Helander, L. Höglund, Pi. Shi, and B. Sundman. Thermo-calc & dictra, computational tools for materials science. *Calphad*, 26(2):273–312, 2002.

[24] B. Sundman, H.L. Lukas, and S.G. Fries. *Computational thermodynamics: the Calphad method*. Cambridge university press, 2007.

[25] D. Bowden, Y. Krysiak, L. Palatinus, D. Tsivoulas, S. Plana-Ruiz, E. Sarakinou, U. Kolb, D. Stewart, and M. Preuss. A high-strength silicide phase in a stainless steel alloy designed for wear-resistant applications. *Nature communications*, 9(1):1–10, 2018.

[26] N. Krendelsberger, F. Weitzer, Y. Du, and J.C. Schuster. Constitution of the ternary system Cr–Ni–Ti. *Journal of alloys and compounds*, 575:48–53, 2013.

[27] S. Ackerbauer, N. Krendelsberger, F. Weitzer, K. Hiebl, and J.C. Schuster. The constitution of the ternary system Fe–Ni–Si. *Intermetallics*, 17(6):414–420, 2009.

[28] M. Kowalski. Polytypic structures of $(Cr,Fe)_7C_3$ carbides. *Journal of applied crystallography*, 18(6):430–435, 1985.

[29] J.P. Morniroli, E. Bauer-Grosse, and M. Gantois. Crystalline defects in M_7C_3 carbides. *Philosophical Magazine A*, 48(3):311–327, 1983.

[30] Ilya M Lifshitz and Vitaly V Slyozov. The kinetics of precipitation from supersaturated solid solutions. *Journal of physics and chemistry of solids*, 19(1-2):35–50, 1961.

[31] Carl Wagner. Theorie der alterung von niederschlägen durch umlösen (ostwald-reifung). *Zeitschrift für Elektrochemie, Berichte der Bunsengesellschaft für physikalische Chemie*, 65(7-8):581–591, 1961.

[32] R.W. CAHN. Chapter 28 - recovery and recrystallization. In *Physical Metallurgy*, pages 2399 – 2500. Elsevier, Oxford, fourth edition edition, 1996.

[33] F.J. Humphreys and M. Hatherly. *Recrystallization and related annealing phenomena*. Elsevier, 2012.

[34] S. Irukuvarghula, H. Hassanin, C. Cayron, M.M. Attallah, D. Stewart, and M. Preuss. Evolution of grain boundary network topology in 316L austenitic stainless steel during powder hot isostatic pressing. *Acta Materialia*, 133:269–281, 2017.

[35] S.V. Nair and J.K. Tien. Densification mechanism maps for hot isostatic pressing (HIP) of unequal sized particles. *Metallurgical Transactions A*, 18(1):97–107, 1987.

[36] W.A. Kaysser, M. Asian, E. Arzt, M. Mitkov, and G. Petzow. Microstructural development and densification during hipping of ceramics and metals. *Powder metallurgy*, 31(1):63–69, 1988.

[37] E.K.H. Li and P.D. Funkenbusch. Hot isostatic pressing (HIP) of powder mixtures and composites: Packing, densification, and microstructural effects. *Metallurgical and Materials Transactions A*, 24(6):1345–1354, 1993.

[38] H.R. Piehler and D.P. Delo. Physical modeling of powder consolidation processes. *Progress in materials science*, 42(1-4):263–276, 1997.

[39] G.A. Fontalvo, R. Humer, C. Mitterer, K. Sammt, and I. Schemmel. Microstructural aspects determining the adhesive wear of tool steels. *Wear*, 260(9-10):1028–1034, 2006.

[40] Anders Gåård. Influence of tool microstructure on galling resistance. *Tribology International*, 57:251–256, 2013.

[41] T Lesage, S Bouvier, M Risbet, and PE Mazeran. In-depth microstructural analysis of galling deformation in stainless steels. *Tribology Letters*, 69(4):1–14, 2021.

APPENDIX A.

MELTING EXPERIMENTS USING DTA

Fig. A-1 depicts two DTA traces for HIPed Tristelle 5183 showing endothermic reactions associated the melting of the γ matrix and dissolution of a hard precipitate phase (M_7C_3) during the heating of the alloy. The onset point denoted T_o, which occurs at a temperature between 1217 and 1220 ^{o}C, corresponds to the onset of melting at the γ-M_7C_3 interface. The small shoulder denoted T_e, situated between 1285 and 1291 ^{o}C, marks what is most probably the complete dissolution of the M_7C_3 phase. As the temperature is raised further beyond this point, the continued adsorption of heat is believed to be associated with the melting of any remaining γ.

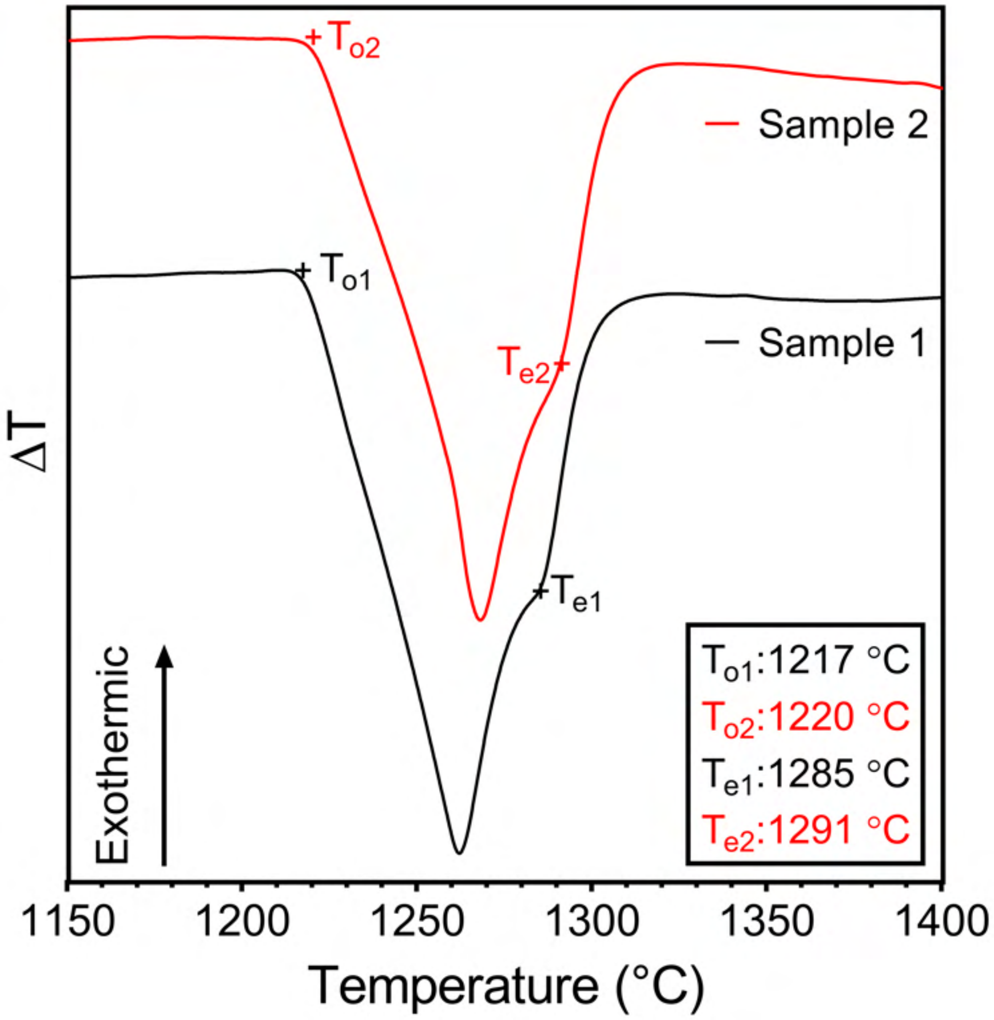

Figure A-1: DTA heating traces for HIPed Tristelle 5183 showing endothermic reactions associated the melting of the γ and dissolution of a hard precipitate phase (M_7C_3).

APPENDIX B.

CALCULATED ISOPLETH DIAGRAMS FOR COMPOSITIONS IN THE REGION OF TRISTELLE 5183

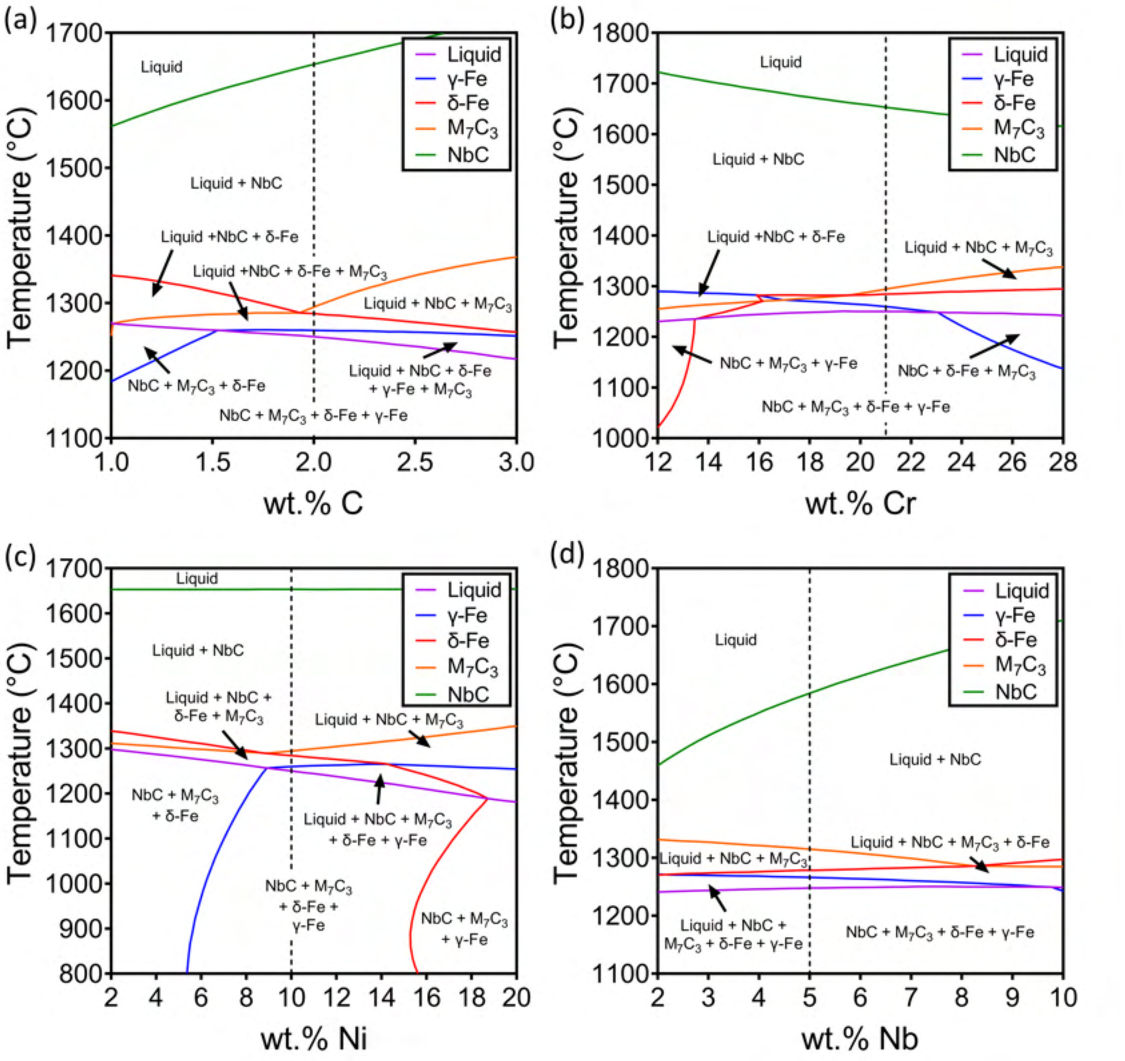

Figure B-1: Isopleth diagrams for Tristelle 5183 showing the effects of varying C (a), Cr (b), Ni (c) and Nb (d) on phase equilibria over a range of temperatures. In each isopleth diagram all compositional variables are kept the same except for the element of interest which is C in (a), Cr in (b), Ni in (c) and Nb in (d)) and the base solvent (Fe). The vertical dashed line in each diagram shows the composition of the alloy in the present work.

LIST OF FIGURES

LIST OF TABLES